CFD Studies of Wake Characteristics and Power Capture of Wind Turbines With Trailing Edge Flaps

WENGUANG ZHANG [ID]1**, YUANYUAN WANG** [ID]2**, YANGZHI SHEN** [ID]2**,**
YANG WANG [ID]2**, YUE XU** [ID]3**, AND XINYU ZHANG** [ID]3

1State Key Laboratory of Alternate Electrical Power System with Renewable Energy Sources, North China Electric Power University, Beijing 102206, China
2School of Control and Computer Engineering, North China Electric Power University, Beijing 102206, China
3China Shipbuilding IT Company Ltd., Beijing 100032, China

Corresponding author: Yuanyuan Wang (turbinewin@gmail.com)

ABSTRACT Trailing edge flap (TEF) devices will change downstream wake development in wind farms comprising smart rotors, which in turn affect the performance of downstream wind turbines. To study the influence of TEFs on downstream wake development and power capture of wind turbines in wind farms, computational fluid dynamics (CFD) simulations using the three-dimensional rotor model are performed in this paper. The CFD software Fluent is adopted to simulate a wind farm with two tandem wind turbines with TEFs at rated and below rated turbulent wind conditions. Under the 11.4 m/s turbulent wind conditions, the results show that the deflection of the TEF increases the velocity deficit and reduces the wake width, making the wake more complicated. And the positive TEF angle has a greater influence on downstream wake than the negative TEF angle. Additionally, under the 9 m/s turbulent wind conditions, the total power of the two wind turbines increases by 6.5% when the TEF angles are 6°.

INDEX TERMS Computational fluid dynamics, horizontal axis wind turbine, power capture, smart rotor, trailing edge flap, wake development.

I. INTRODUCTION

In recent years, as wind power has advanced rapidly, the size of wind turbines and wind farms increase as well to maximize the wind resources with limited available lands [1]. However, large blades aggravate the fatigue and extreme loads on wind turbines within their lifespan, leading to increases in weight, cost of components, and control difficulty [2]. The traditional pitch control can adjust the aerodynamic properties of the blades by changing their pitch angles for load reduction. As wind turbine blades become larger and more flexible, there is an increasing need for locally distributed control surfaces [3]–[5]. Smart rotor technologies for load reduction have been proposed [6]. Among such technologies, trailing edge flap (TEF), a local active aerodynamic load control device, is receiving significant attention owing to its simple structure and excellent high-frequency regulating

capability [7]. In smart rotor operation, TEFs can modify the aerodynamic properties of the airfoil by changing its camber, making it possible to compensate for the loads variations caused by the fluctuating local wind speeds seen by the rotating blade [4]. Currently, adding TEFs to a blade is one of the most promising methods to achieve load alleviation for large wind turbines.

Many researchers have investigated the TEF control performance from the perspectives of load alleviation and power capture [7]–[29]. Basualdo [8] conducted a two-dimensional theoretical study of the aeroelastic behavior of an airfoil with geometry that could be altered using a rear-mounted flap. The results showed that the use of variable airfoil geometry is an effective means of reducing the vibration magnitude of an airfoil. Bak *et al.* [9] carried out a wind tunnel test of the wind turbine Risø-B1-18 airfoil, which is equipped with an adaptive trailing edge geometry. The results demonstrated that it is possible to control the loads on a wind turbine airfoil with an adaptive trailing edge geometry. At Risø

DTU in Denmark, a continuous research of using TEFs for reducing load fluctuations has been carried out [10]–[12]. Additional investigations of TEF devices are underway worldwide. At Sandia National Laboratories, a rotor with integrated sensors and rigid TEFs installed on the 9 m-long blades has been designed, built and tested, ultimately showing that TEFs can reduce microstrains effectively while the output power is reduced to a certain extent [13], [14]. Lackner and van Kuik [6] investigated the load reduction capabilities of TEFs in the operation of a 5 MW wind turbine. A feedback control approach was implemented for load reduction based on multiblade coordinate transformation and the use of TEFs was shown to reduce the fatigue loads on blades effectively. Zhang *et al.* [15] developed a wind turbine model with TEFs based on an unsteady aerodynamic model. They implemented a TEF controller using a feedback linearization-based control method and the results showed that the model has good reliability and that the use of a feedback-linearization-based TEF controller can reduce fatigue load and smooth output power. Zhang *et al.* [7] established an exact smart rotor model with TEFs by considering aerodynamic damping and bend-twist coupling and designed multi-objective robust adaptive tracking (RAT) controllers for TEFs. The results showed that the RAT control method can suppress the fluctuations of flapwise tip deflection and output power for smart rotors with TEFs, and the method can also be applied to counter dramatic changes in time-varying nonlinear systems.

In addition, some studies have focused on the optimization of TEF sizing parameters. Smit *et al.* [26] investigated the effects of the sizing and location of flap configuration on a possible increase in energy production and concluded that flap elements near the blade tip are the most effective. Zhang *et al.* [27] developed a wind turbine model with smart rotor and validated it by comparing with FAST [28]. Additionally, they proposed an approach to optimize TEF sizing parameters to maximize TEF effects on blade load alleviation and wind turbine output power smoothness. Their approach utilized two orthogonal experiments, and then the optimal group of TEFs sizing parameters was validated via estimation approaches. Andersen *et al.* [29] adopted strain gauges as inputs for a flap controller and investigated the effects of placing strain gauges at various radial positions on a blade. Furthermore, they utilized an optimization routine that minimizes blade root fatigue loads.

Computational fluid dynamics (CFD) is capable of modeling complex three-dimensional flow fields accurately and simulating fluid dynamics reliably [30], [31]. Therefore, several CFD studies on TEFs have been implemented recently. Jost *et al.* [32] presented an overview of different possibilities for realizing actively deflecting flaps based on CFD. A model based on grid deformation was considered to be favorable because fewer grid cells were needed and greater accuracy was achieved compared to the CHIMERA [32] approach. Jawahar *et al.* [33] studied the aerodynamic performance of a NACA 0012 airfoil fitted with different flaps.

The results revealed that flap camber profiles significantly affect aerodynamic performance and the downstream wake development of airfoils.

Overall, the studies above mainly focused on single wind turbine with TEFs. The results indicate that TEF control can reduce load and affect output power. The main utilization of wind energy is in the form of large-scale wind farms for grid-connected power generation, especially in China [27]. When a wind turbine operates in the lee of another turbine in a large wind farm, it incurs wake penalty. The average energy loss caused by wind turbine wakes is approximately 10% to 20% of annual energy production. Additionally, the wake of a wind turbine can have a detrimental effect not only on performance but also on the fatigue loads of downstream wind turbines [34]. TEF devices will change downstream wake development in wind farms consisting of smart rotors, which in turn influence the performance of downstream wind turbines. However, very few studies have considered this aspect of TEFs.

In this paper, to study the influence of TEFs on the downstream wake development and power capture of wind turbines in wind farms, CFD simulations of two smart rotors aligned in a line using the three-dimensional rotor model are performed. At rated wind speed, the influence of different TEF angles of upstream wind turbine on downstream wake development and power of the two wind turbines is studied. The power capture of two wind turbines with TEFs at below rated wind speed is also investigated.

The remainder of this paper is organized as follows. In Section II, a numerical model is presented, along with a smart rotor model with TEFs, computational domain, boundary conditions, and grid setup. Section III discusses the verification of the computational results including the grid independence and the output power verification. Section IV presents the results and discussions, including the analysis of velocities, turbulences, flow structures of the wake, and output power. Finally, Section V concludes this paper.

II. NUMERICAL MODEL

In this research, a National Renewable Energy Laboratory (NREL) 5 MW reference wind turbine [35] is selected as the modeling object and one TEF is added to each blade. The CFD software Fluent 18.0 [36] is used to simulate a wind farm with two smart rotors with TEFs.

A. MODELING OF SMART ROTORS WITH TEFs

1) REFERENCE WIND TURBINE

In this study, simulations are performed using the 5 MW reference wind turbine. Designed by the NREL with a rotor diameter of 126 m, the size of the NREL 5 MW wind turbine can be considered as close to the current average rotor size of newly installed wind turbines which accounts to 100 m-120 m [37]. Table 1 provides an overview of the relevant dimensions and operating conditions for the NREL 5 MW reference wind turbine.

TABLE 1. Parameters of the NREL 5 MW wind turbine.

Parameters	Values
Rating Power	5.4 MW
Rotor Orientation	Upwind
Rotor Diameter	126 m
Hub Diameter	3 m
Rotor Mass	110000 kg
Blade Mass	17740 kg
Structural-Damping Ratio	0.477465%
Rated Rotor Speed	12.1 rpm
Rotor Configuration	3 Blades
Cut-In Wind Speed	3 m/s
Rated Wind Speed	11.4 m/s
Cut-Out Wind Speed	25 m/s

TABLE 2. Parameters of the TEFs.

Parameters	Values
Chord length ratio	25%
Maximum deflection Angle	±10°
Length	14.35 m
Position	45.10 m-59.45 m
Airfoil	NACA64_A17

2) TEF DESCRIPTION

The optimal parameters of the TEFs are obtained from two orthogonal experimental designs [27]. A TEF is added to each blade and the details of the TEFs are provided in Table 2. The TEFs are treated as rigid bodies. The structure of a NREL 5 MW wind turbine blade with TEFs is presented in Fig. 1.
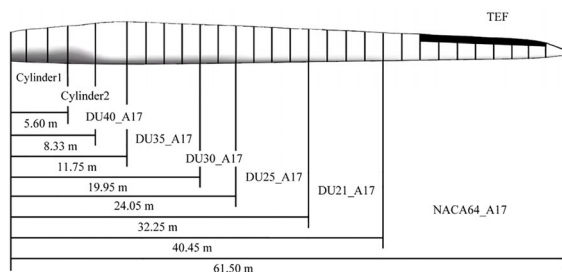

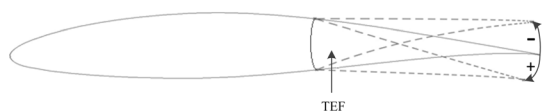**FIGURE 1. Structure of NREL 5 MW wind turbine blade with a TEF.**

FIGURE 2. Motion direction diagram of the TEF.

The motion direction of the TEF is shown in Fig. 2. The TEF moves in the direction of the ''+'' arrow (i.e., clockwise)
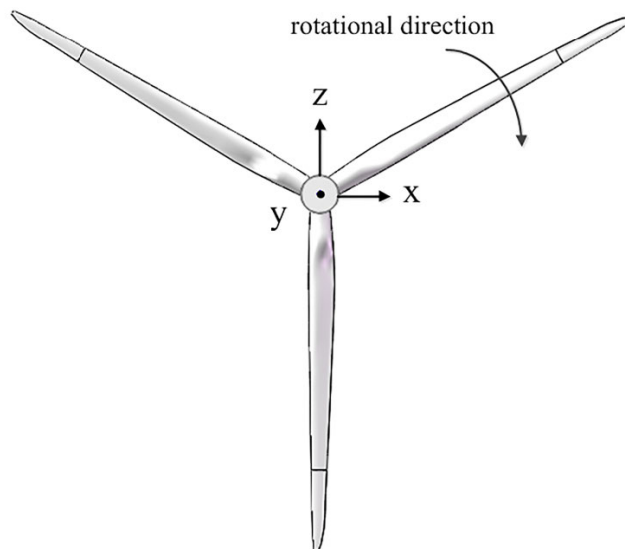

FIGURE 3. Model of a smart rotor with TEFs.

for the positive direction and in the direction of the ''−'' arrow (i.e., counterclockwise) for the negative direction.

The smart rotor with TEFs is presented in Fig. 3 with the relevant coordinate system and rotational direction. The nacelle and tower will affect the wake characteristics and have strong interaction with the blades and TEFs [38]–[42]. In this paper, in order to isolate study the influence of TEFs on the wake characteristics, the nacelle and tower are not included in the CFD model of wind turbines. The blade has a length of 61.5 m and the blade pitch and yaw angles are fixed at 0° for all performed simulations.

B. COMPUTATIONAL DOMAIN AND BOUNDARY CONDITIONS

When the placement of two smart rotors is in a line with TEFs, the influence of the TEFs on the downstream wind turbine is the largest, and the flow field in other placement of two smart rotors can be approximately calculated by formulas [43]. The power production and lifetime of a downstream turbine are heavily affected by the separation distance between wind turbines [1]. Choi *et al.* [44] examined separation distances ranging from 3D to 7D and found that the performance of a downstream wind turbine decreases notably when the separation distance is less than 6D, where D is the rotor diameter. Hence, a 7D separation distance, which is typical for downstream turbines in modern wind farms, is chosen for simulation. In this paper, the upstream and downstream wind turbines are denoted as wind turbine one (WT1) and wind turbine two (WT2), respectively.

As shown in Fig. 4, the computational domain is a cylindrical zone with a base radius of 3D and a height of 19D. It is composed of three main zones, the far-field zone, which is a stationary zone, and two internal zones composed of two rotational parts including two rotors with independent coordinate
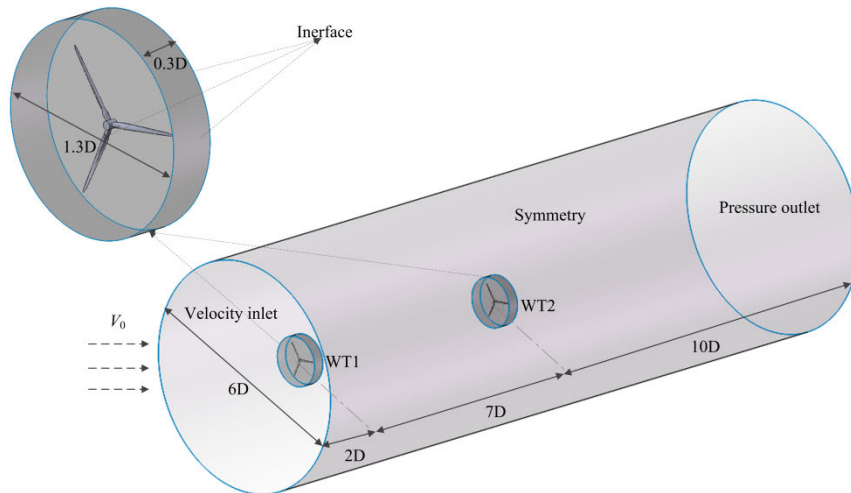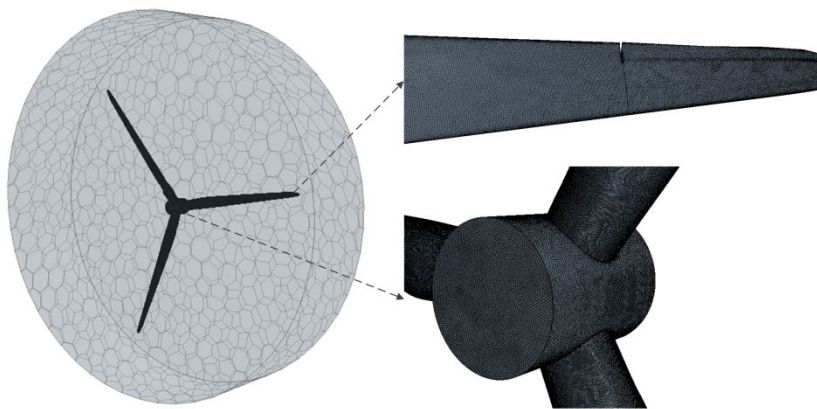
FIGURE 4. The computational domain.

FIGURE 5. Mesh of the rotational domain.

systems for rotation. The rotational parts are cylindrical zones with a diameter of 1.3D and height of 0.3D.

Fig. 4 presents the boundary conditions used in our simulations. A uniform wind speed with 5% turbulence intensity is set at the inlet of the domain in the following simulations. The boundary conditions for the side surface of the domain is a symmetrical wall to ensure zero-gradient conditions for the scalar quantities tangential components of vector quantities, and be zero for the normal component of vector quantities [1]. The contact surfaces between the rotational and the stationary domain are configured as interfaces. A moving reference frame technique is applied to these interfaces. A pressure outlet condition is assigned to the outlet of the domain with a value of 0 Pa. The blade surfaces are configured as no-slip walls.

C. GRID SETUP

Due to the complex geometry of smart rotors with TEFs, the commercial CFD package STAR-CCM+ 11.02 [45] is adopted to construct polyhedral meshes in the two

rotational domains. The final meshes and local magnifications are presented in Fig. 5. A polyhedral type mesh, which is able to reduce the number of cells by approximately 50% compared to a hexahedral type mesh of the same size while offering superior robustness of convergence, is used to fill whole regions. Local volume refinement zones are used in the vicinity of the blade and in the wake region immediately downstream of the blade to maintain a high resolution in those areas. The minimum mesh size of the blade is 0.01 m and the maximum mesh size is 0.1 m. The blade surface is covered by a prism grid to ensure the accuracy of boundary layer flow simulation. All wall surfaces of the wind turbine are covered with eight layers of boundary meshes to ensure appropriate wall treatment. Finally, the thickness of the first layer mesh on the blade tip is 0.0006 m, the growth ratio of the layer is 1.2, and the total thickness of the boundary mesh is 0.01 m.

Because the far-field zone is simple in structure, ICEM 18.0 [46] is utilized to construct hexahedral meshes in the stationary domain. The final mesh and local magnifications are presented in Fig. 6.
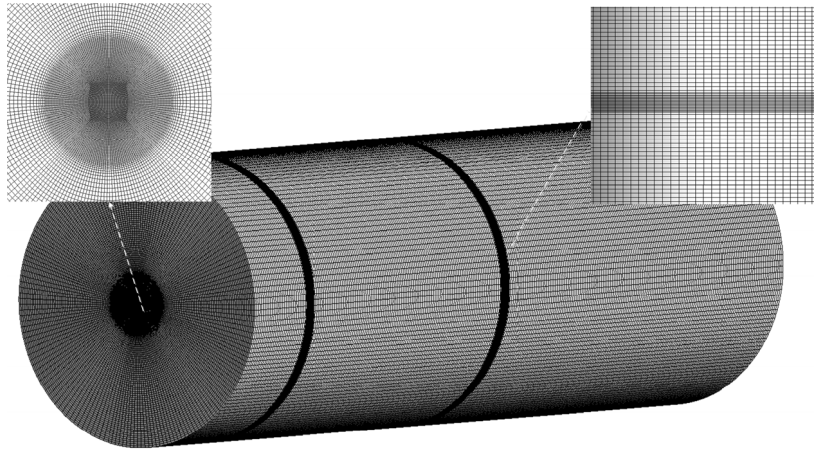
FIGURE 6. Mesh of the stationary domain.

The grid numbers for each rotational domain and stationary domain are 6.37 million and 6.21 million, respectively, with a total number of cells of 18.95 million. The results of mesh independence tests will be presented later.

D. NUMERICAL METHODS

Considering the calculation cost and the weak interaction between the rotational zones and the external stationary zone, a steady incompressible numerical simulation method is used for wind field simulation. The flow field is low-speed incompressible, which is solved by the implicit three-dimensional solver based on pressure separation. The Reynolds-Averaged Navier-Stokes equations (RANS) are solved using Fluent. In Cartesian coordinates, the three-dimensional steady RANS equations for steady incompressible flows include the following equations:

The continuity equation:

$$\frac{\partial(\rho u_i)}{\partial x_i} = 0 \tag{1}$$

The momentum equation:

$$\frac{\partial(\rho u_i u_j)}{\partial x_i} = \frac{\partial P}{\partial x_i} + \frac{\partial}{\partial x_i}\left[\mu\frac{\partial u_i}{\partial x_i} + \frac{\partial u_j}{\partial x_i} - \rho\overline{u_i'u_j'}\right] \tag{2}$$

where u_i and u_j are the average speed components; x_i and y_j are the coordinate components; $i, j = 1, 2, 3$; P is the fluid average pressure; μ is the kinematic viscosity coefficient of the fluid; and ρ is the fluid density.

In the momentum equation, the expression $\rho\overline{u_i'u_j'}$ is known as Reynolds stress and denotes the effects of turbulence. For a viscous flow, the Reynolds stress is unknown. Hence, in order to solve the momentum equation, a turbulence model must be used to simulate the Reynolds stress term.

Complex flows are considered in the $k-\omega$ model under adverse pressure gradient in the near-wall region, and the $k-\varepsilon$ turbulence model is favorable for the full rotor simulation. The shear stress transport (SST) $k-\omega$ turbulence model effectively combines aptitudes of the $k-\omega$ model and the

$k-\varepsilon$ turbulence model. Consequently, the $k-\omega$ transitional SST turbulent model is used for turbulence modeling.

The SST model is formulated as follows:

$$\frac{\partial(\rho k)}{\partial t} + \frac{\partial(\rho U_i k)}{\partial x_i} = \widetilde{P}_k - \beta^*\rho k\omega + \frac{\partial}{\partial x_i}\left[(\mu+\sigma_k\mu_t)\frac{\partial k}{\partial x_i}\right] \tag{3}$$

$$\frac{\partial(\rho\omega)}{\partial t} + \frac{\partial(\rho U_i\omega)}{\partial x_i} = \alpha\rho S^2 - \beta\rho\omega^2 + \frac{\partial}{\partial x_i}\left[(\mu+\sigma_\omega\mu_t)\frac{\partial\omega}{\partial x_i}\right]$$
$$+ 2(1-F_1)\rho\sigma_{\omega 2}\frac{1}{\omega}\frac{\partial k}{\partial x_i}\frac{\partial\omega}{\partial x_i} \tag{4}$$

where the blending function F_1 is defined as follows:

$$F_1 = \tanh\left\{\left\{\min\left[\max\left(\frac{\sqrt{k}}{\beta^*\omega y}, \frac{500v}{y^2\omega}\right), \frac{4\rho\sigma_{\omega 2}k}{CD_{k\omega}y^2}\right]\right\}^4\right\} \tag{5}$$

where $CD_{k\omega} = \max\left(2\rho\sigma_{\omega 2}\frac{1}{\omega}\frac{\partial k}{\partial x_i}\frac{\partial\omega}{\partial x_i}, 10^{-10}\right)$ and y are the distances to the nearest wall. F_1 is equal to zero in the area away from the surface ($k-\varepsilon$ model) and switches to a value of one inside the boundary layer ($k-\omega$ model).

The turbulent eddy viscosity is defined as follows:

$$v_t = \frac{a_1 k}{\max(a_1\omega, SF_2)} \tag{6}$$

where S is an invariant measure of the strain rate and F_2 is a second blending function defined as follows:

$$F_2 = \tanh\left[\left[\max\left(\frac{2\sqrt{k}}{\beta^*\omega y}, \frac{500v}{y^2\omega}\right)\right]^2\right] \tag{7}$$

A production limiter is utilized in the SST model to prevent the build-up of turbulence in stagnation regions as follows:

$$P_k = \mu_t\frac{\partial U_i}{\partial x_j}\left(\frac{\partial U_i}{\partial x_j} + \frac{\partial U_j}{\partial x_j}\right) \rightarrow \widetilde{P}_k = \min(P_k, 10\cdot\beta^*\rho k\omega) \tag{8}$$

A thorough explanation of numerous blending functions and corresponding constants for the SST turbulence model is provided by Menter [47].

Absolute is selected for velocity formulation. The moving reference frame technique is adopted for data exchange between the rotational zones and stationary zone. The angular velocity of the rotational zones is set firstly, then the rotating axis is set as y-axis and the speed of the blade relative to the rotating zones is set to 0 rpm. SIMPLE algorithm is chosen for Pressure-Velocity coupling scheme because the flow is assumed as steady. To improve the calculation accuracy, second order upwind discretization is chosen for momentum equation, turbulent kinetic energy and dissipation rate. The number of iterations is set to 1200, and the residual and moment of smart rotors with TEFs are monitored in the simulations. Convergence is deemed sufficient when the residual is less than 10^{-5} or the moment of the blade is near to steadiness.

III. VERIFICATION OF COMPUTATIONAL RESULTS

Under the 11.4 m/s turbulent wind conditions, the grid independence of one wind turbine based on a fixed 0° TEF angle is validated. Then, the output power calculated by Fluent is compared to the results of FAST at different wind speeds.

A. GRID INDEPENDENCE

Table 3 lists the different torque calculated for five different numbers of cells. The grid numbers are computed for the k-ω transitional SST turbulent model and simulations are performed with the following grid numbers: 11.35 million, 12.67 million, 15.01 million, 18.95 million, and 23.57 million. For the condition without TEFs, the designed torque at 11.4 m/s wind speed is approximately 4.08 MN·m, which is used as a reference value. The relative error for a mesh with 18.95 million cells is less than 5% and the computational cost of using such a mesh is moderate. Therefore, this mesh is selected for further investigation.

TABLE 3. Computed torques for different grid sizes.

Numbers of Cells (Millions)	Torque (MN·m)	Relative error
11.35	3.49	14.35%
12.67	3.52	13.63%
15.01	3.76	7.78%
18.95	3.88	4.90%
21.97	4.02	1.47%
26.21	4.16	2.00%

B. OUTPUT POWER VERIFICATION

The output power of a wind turbine is estimated based on the clockwise torque of its rotor as follows:

$$P = M \frac{n \cdot 2\pi}{60} \qquad (9)$$

where P is the output power (W), M is the torque of the rotor (N·m), and n is the rotor speed (rpm).
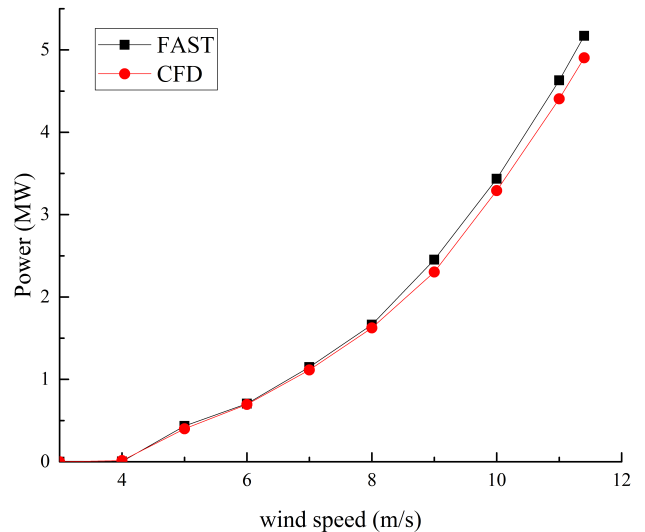

FIGURE 7. Comparison of output power between FAST and CFD simulations at different wind speeds.

Several steady simulations with wind speeds ranging from the cut-in wind speed of 3 m/s to the rated wind speed of 11.4 m/s are tested and the results are compared to the results of the FAST, as presented in Fig. 7. The corresponding rotor speeds for each wind speed are defined in [35]. The blades must adjust their pitch angles when the wind speed exceeds the rated speed, so excessive wind speeds are not considered in this study. Since the calculations of FAST based on the blade element method, which lacks three-dimensional flow effects around blades, the output power calculated by FAST is slightly greater than that calculated by CFD simulations [1].

IV. RESULTS AND DISCUSSION

Under the 11.4 m/s turbulent wind conditions, the influence of WT1's different TEF angles on downstream wake development and the output power of WT1 and WT2 in a wind farm is studied. Eleven simulations are performed with WT1's TEF angles of 0°, ±2°, ±4°, ±6°, ±8°, and ±10°, and WT1's TEF angles of 0°. Under the 9 m/s turbulent wind conditions, the power capture of the two wind turbines with TEFs is also investigated. Two simulations are performed with WT1's TEF angles of 0° and 6°. The thirteen simulations described above are denoted as Case1 to Case13. Table 4 lists the TEF angle settings for the different cases.

Under the 11.4 m/s turbulent wind conditions, the corresponding rotor speed of WT1 is 12.1 rpm. Because of the influence of the upstream wake, the wind speed experienced by WT2 is much lower than 11.4 m/s. Consequently, in order to maintain a relatively high power coefficient, the rotation speed of WT2 is set to 8 rpm in the first eleven simulations. Similarly, in the two simulations at the 9 m/s turbulent wind conditions, the corresponding rotor speeds of WT1 and WT2 are 10.3 rpm and 6.9 rpm, respectively.
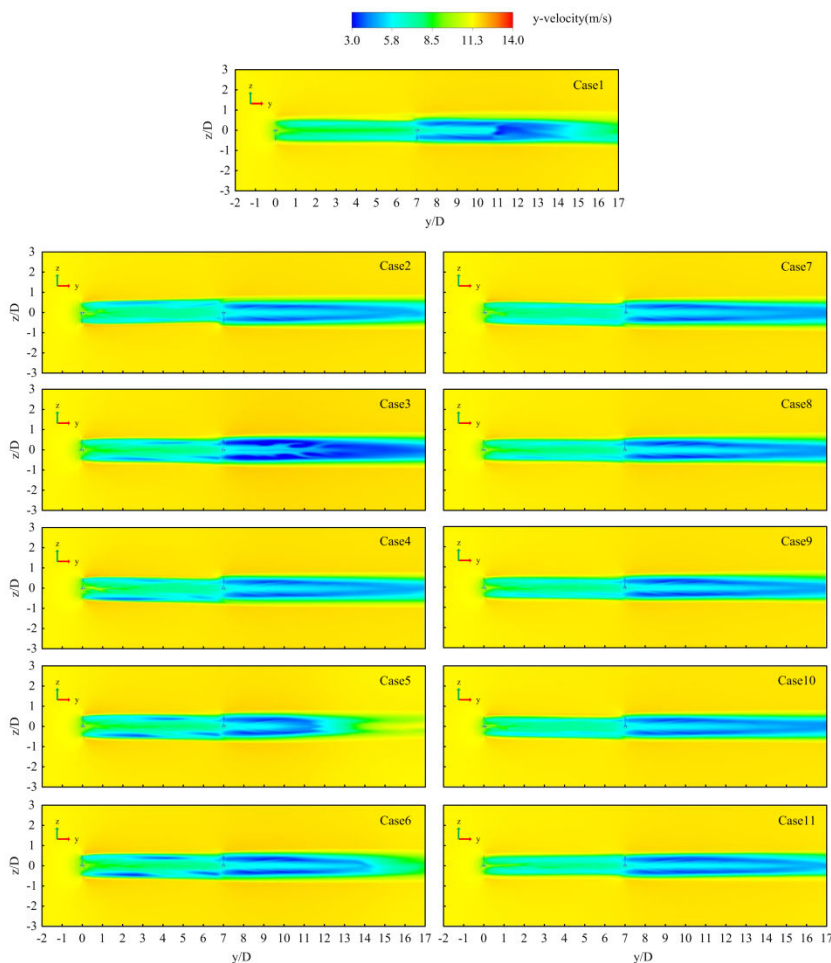
FIGURE 8. Horizontal y-velocity profiles at the center of the hub (x = 0) in Case1 to Case11.

TABLE 4. TEF angle settings for different cases.

Cases	TEF angles of WT1 (°)	TEF angles of WT2 (°)	Wind speed (m/s)
Case1	0	0	11.4
Case2	+2	0	11.4
Case3	+4	0	11.4
Case4	+6	0	11.4
Case5	+8	0	11.4
Case6	+10	0	11.4
Case7	-2	0	11.4
Case8	-4	0	11.4
Case9	-6	0	11.4
Case10	-8	0	11.4
Case11	-10	0	11.4
Case12	0	0	9.0
Case13	+6	+6	9.0

Velocity deficit can be utilized to analyze the level of velocity recovery and wake width, which indicates the influential area of wake expansion. As a result, velocity is usually considered in the analysis of horizontal axis wind turbine wake.

A. VELOCITY PROFILES IN THE WAKE

The vertical y-velocity profiles at the center of the hub (x = 0) and corresponding y-velocity contours in the near downstream area behind WT1 are shown in Figs. 8 and 9, respectively. TEF deflection causes a greater velocity deficit and longer low-velocity zone. This influence is more pronounced when the TEF angle is positive, as shown in Fig. 8. In Fig. 9, the effects of TEFs on the near downstream wake behind WT1 can be observed more clearly. In all cases other than Case11, there are two high-speed zones at the edge of the wake caused by TEF deflection. The range of the high-speed zone with positive TEF angles is greater than that of the zone with negative TEF angles. Additionally, in Case2 to Case11 which have TEF deflection, the velocity loss is greater and the flow of the wake is more complex than that of the 0° TEF angles in Case1. The flow is also more complicated when the TEF angles are positive. It can be seen that different TEF angles have a significant influence on downstream velocity distributions and that positive TEF angle plays a greater role.

In the range of $-1.5 \leq z / D \leq 1.5$ and at the center of the hub (x = 0), the vertical profiles of normalized axial
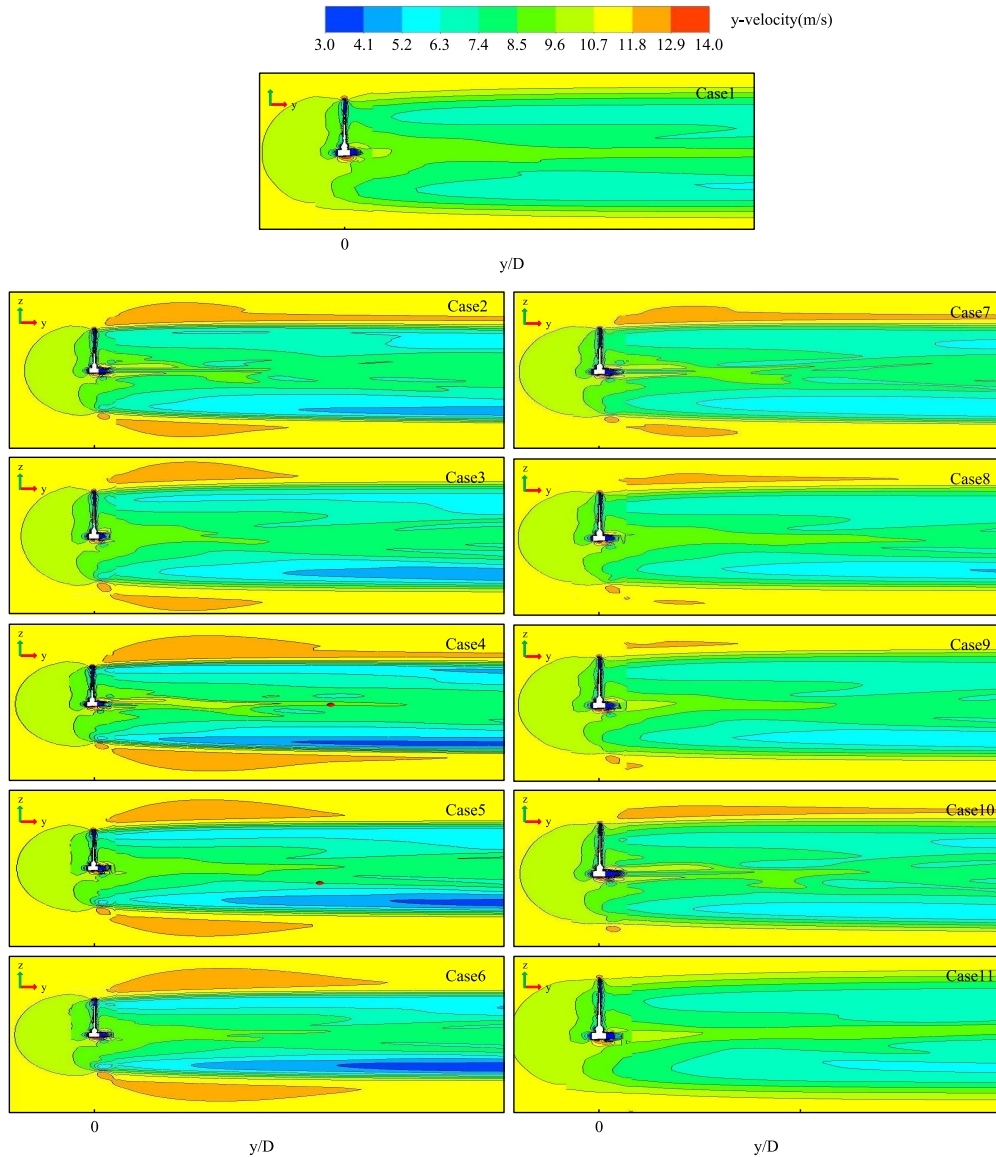
FIGURE 9. Horizontal y-velocity contours in the near downstream wake behind WT1.

velocities are presented in Fig. 10. The axial velocity V_y is normalized by the corresponding reference wind speed V_{ref}. Therefore, the normalized velocities at the upstream station are equal to 1. These results reveal the velocity deficit caused by the momentum extraction of the wind turbine and the consequent recovery behind the wind turbine. Owing to the stagnation effect and the consequent expansion of stream tube, the normalized velocities are not equal to 1 at the upstream location of y / D = −1. In Case2 to Case6 where the TEF angles are positive, the velocity is always less than that in Case1 where the TEF angles are 0°. And the velocity decreases as the angle increases. In contrast, when the TEF angles are negative, the velocity increases with the angle, even more than those when the TEF angles are 0°. As shown in Fig. 10, near-symmetrical behavior of the velocity profiles

can be observed about the hub center corresponding to the rotor blade at y / D = −1, 8, 10, 12, 14, 16. However, an asymmetrical and more complicated velocity profile can be observed in the near downstream region behind WT1 at y / D = 1, 3, 5. In the case of TEF deflection, the wake velocity in the downstream region behind WT1 is less than that when the TEF angles are 0°, except for the velocities at y / D = 1, 12, 14, 16, which are locations near and relatively far from WT1.

B. FLOW STRUCTURES OF THE WAKE
The vertical y-velocity profiles at different stream-wise locations in the first eleven cases (Table 4) are presented in Fig. 11. The width of the wake is defined as the region in which the ratio of velocity profile value to inflow wind speed
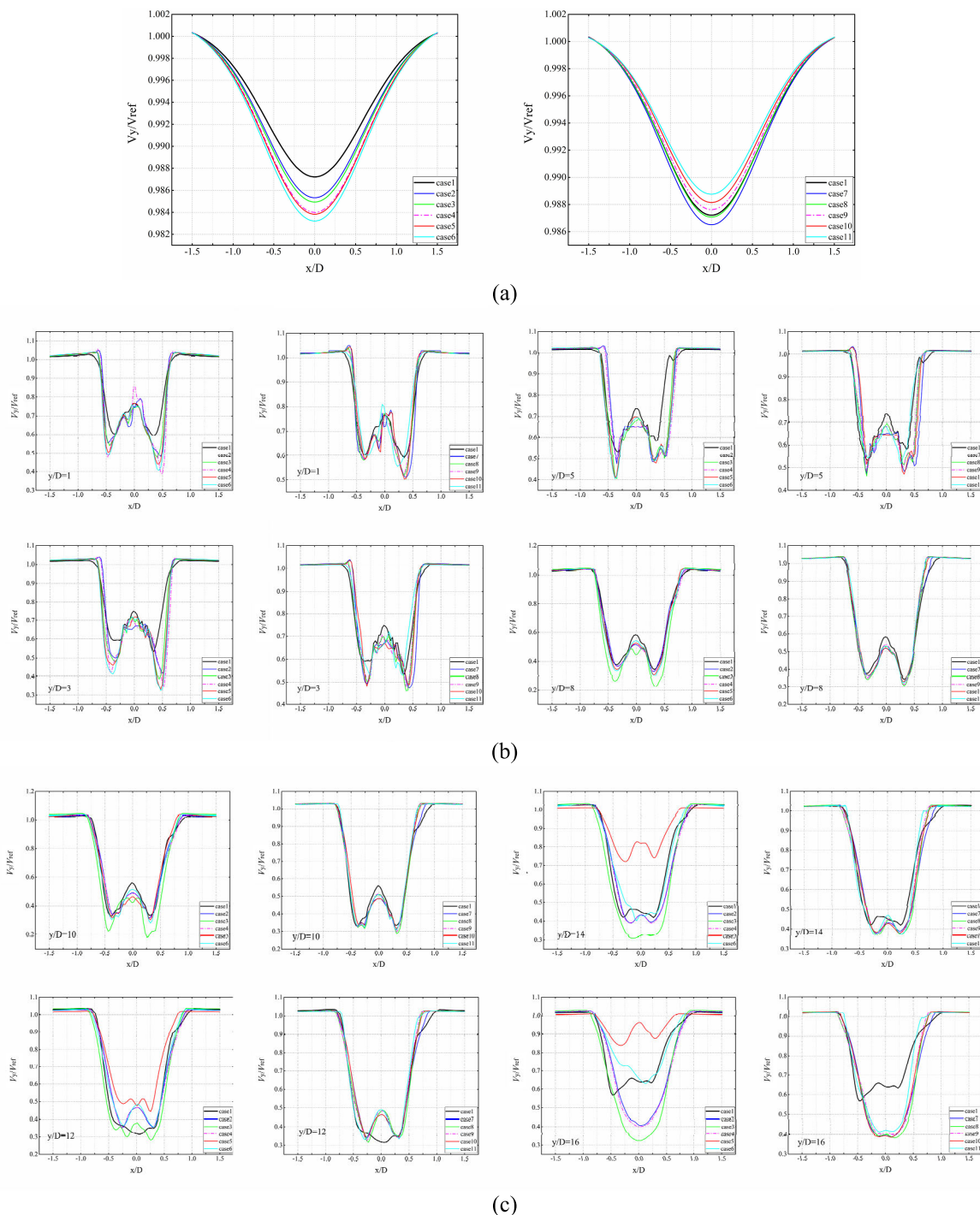
FIGURE 10. Comparison of normalized y-velocities at one upstream and eight downstream locations.

is smaller than 0.99 [48], which is denoted by the arrows in Fig. 11.

From the velocity profiles at y / D = 1, 3, 5 in these eleven cases (Table 4), it can be seen that the wake widths behind WT1 in Case2 to Case11 are smaller than that in Case 1, but the corresponding velocity deficits are greater. In Case2 to Case6 where the TEF angles are positive, the velocity deficit increases with angle. In contrast, in Case7 to Case11 where the TEF angles are negative, the velocity deficit decreases with angle. The wake is approximately symmetrical about the centerline and maintains a circular shape with increasing downstream distance in Case1. However, the wake exhibits asymmetrical behavior and gradually transforms into a triangle shape in Case2 to Case11.
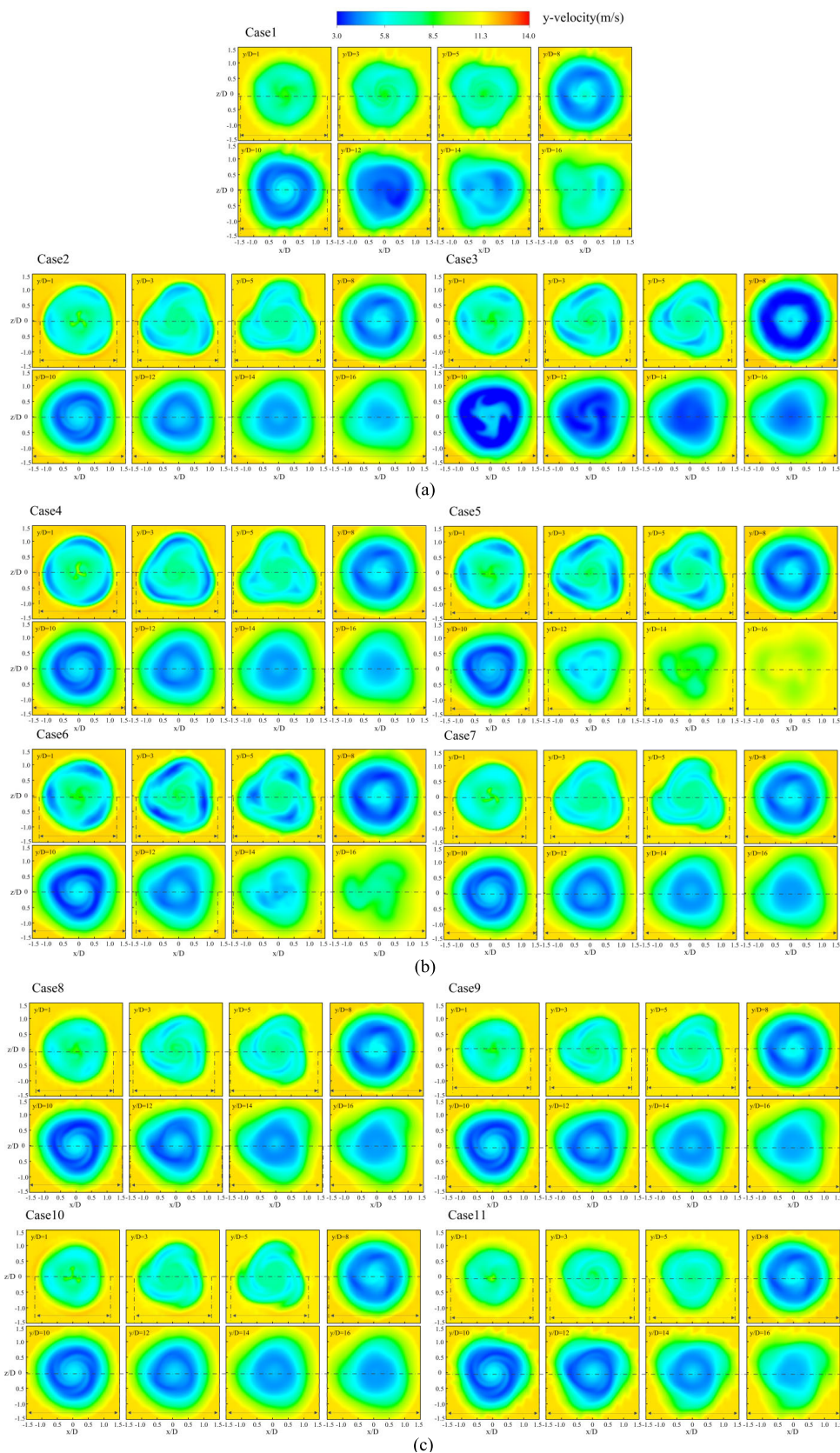
FIGURE 11. Vertical y-velocity profiles at different stream-wise locations in Case1 to Case11.

From the velocity profiles at y / D = 8, 10, 12, 14, 16 in these eleven cases (Table 4), because the arriving upstream wake combines with the wake generated by WT2, wakes in all eleven cases enlarge their regions and become more complicated. It can be seen that the wake widths behind WT2 in Case2 to Case11 are not significantly different from that in Case1, except that the velocity deficits are greater than that in Case1.

C. OUTPUT POWER

A comparison of output power for the first eleven cases (Table 4) is presented in Fig. 12. The output power of WT1 in Case1 is 4.84 MW, which satisfies the design standard [35] and verifies the validations of present simulations in another way. When the TEF angles are negative, the output power of WT1 decreases as angle increases. When the TEF angles are positive, the power of WT1 is greater than that with a 0° TEF angle, as shown in Fig. 12.
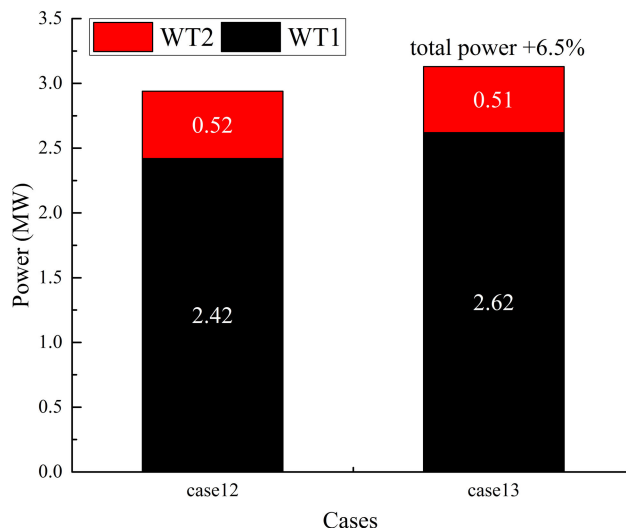

FIGURE 13. Output power comparison between Case12 and Case13.

TABLE 5. Total output power and growth rate in eleven cases.

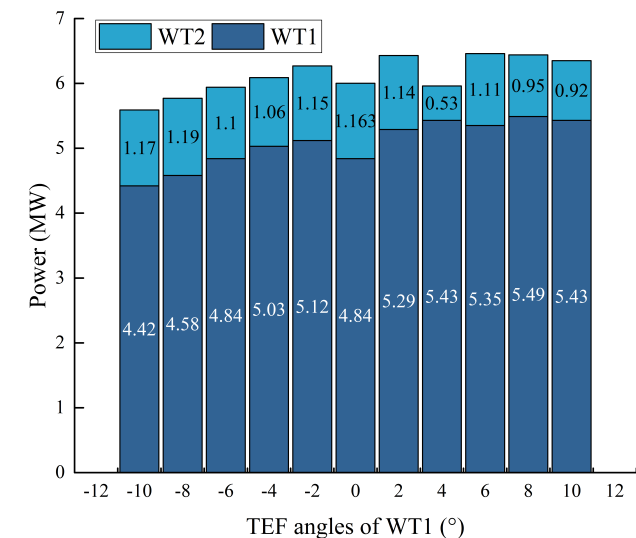| Cases (TEF angles of WT1)	Total power (MW)	Growth rate
Case1 (0º)	6.01	Reference value
Case2 (2º)	6.44	+7.2%
Case3 (4º)	5.96	-0.8%
Case4 (6º)	6.47	+7.6%
Case5 (8º)	6.43	+7.0%
Case6 (10º)	6.35	+5.7%
Case7 (-2º)	6.03	+0.4%
Case8 (-4º)	5.87	-2.4%
Case9 (-6º)	6.09	+1.3%
Case10 (-8º)	5.56	-7.5%
Case11 (-10º)	5.39	-10.3%

FIGURE 12. Comparison of output power in eleven cases.

The total output power of WT1 and WT2, as well as the growth rates in eleven cases (Table 4), are listed in Table 5. When the WT1's TEF angles are 6°, the total power growth rate of the wind turbine reaches 7.6%. The influence of different TEF angles on the total output power can be clearly observed in Table 5. It can be obtained that it is feasible to use TEFs to improve the power capture of wind turbines.

Under the 9 m/s turbulent wind conditions, the TEFs of WT1 and WT2 are deflected by 6° to increase the total power of WT1 and WT2. Fig. 13 presents an output power comparison between Case12 and Case13. When the WT2's TEF angles are set to 6°, the power of WT2 is very close to that of WT2 in Case1 and the total power growth rate of WT1 and WT2 is 6.5%. Overall, the simulations demonstrate the ability to improve the power capture of smart rotors with TEFs.

Most importantly, different TEF angles have a significant influence on downstream wake development and the positive TEF angles play a greater role. Additionally, smart rotors with TEFs can be utilized to improve the output power of wind farms.

V. CONCLUSION

In this paper, the influence of TEFs on the downstream wake development and power capture of wind turbines with TEFs in wind farms is analyzed based on CFD simulations of two smart rotors with TEFs aligned in a line using the three-dimensional rotor model. The following conclusions can be drawn from the present study:

1) Several steady simulations from the cut-in wind speed of 3 m/s to the rated wind speed of 11.4 m/s are tested and the results are compared to those of FAST. The simulation results show good agreement with the FAST results, indicating that the three-dimensional rotor model is capable of simulating the operational processes of wind turbines with TEFs accurately.

2) At the rated wind speed, the influence of TEF angles on downstream wake development is studied. The results show that the deflection of the TEF increases the velocity deficit and reduces the wake width, making the wake more complicated. And the positive TEF angle has a greater influence on downstream wake than the negative TEF angle. The downstream wake exhibits asymmetrical behavior and transforms into a triangle shape gradually in the presence of TEF deflection.

3) The power capture of two wind turbines with TEFs is investigated. The total power growth rate of the wind turbine reaches 7.6% at the 11.4 m/s wind speed, when the TEFs of WT1 and WT2 are deflected by 6° and 0°, respectively. The total power growth rate of WT1 and WT2 is 6.5% at the 9 m/s wind speed, when the TEFs of WT1 and WT2 are both deflected by 6°. These results demonstrate that it is feasible to use smart rotors with TEFs to improve the output power of wind farms.

Overall, our CFD analysis of TEF angles reveals their considerable influence on the wake characteristics and output power of wind turbines, which should provide a useful reference for wind farm control.

REFERENCES

[1] W. Miao, C. Li, G. Pavesi, J. Yang, and X. Xie, "Investigation of wake characteristics of a yawed HAWT and its impacts on the inline downstream wind turbine using unsteady CFD," *J. Wind Eng. Ind. Aerodyn.*, vol. 168, pp. 60–71, Sep. 2017, doi: 10.1016/j.jweia.2017.05.002.

[2] D. Castaignet, I. Couchman, N. K. Poulsen, T. Buhl, and J. J. Wedel-Heinen, "Frequency-weighted model predictive control of trailing edge flaps on a wind turbine blade," *IEEE Trans. Control Syst. Technol.*, vol. 21, no. 4, pp. 1105–1116, Jul. 2013, doi: 10.1109/tcst.2013.2260750.

[3] T. Barlas and G. Van Kuik, "Review of state of the art in smart rotor control research for wind turbines," *Prog. Aerosp. Sci.*, vol. 46, no. 1, pp. 1–27, Jan. 2010, doi: 10.1016/j.paerosci.2009.08.002.

[4] I. Couchman, D. Castaignet, N. K. Poulsen, T. Buhl, J. J. Wedel-Heinen, and N. A. Olesen, "Active load reduction by means of trailing edge flaps on a wind turbine blade," presented at the Amer. Control Conf., Portland, OR, USA, Jun. 2014.

[5] X. Wang, Z. Ye, S. Kang, and H. Hu, "Investigations on the unsteady aerodynamic characteristics of a horizontal-axis wind turbine during dynamic yaw processes," *Energies*, vol. 12, no. 16, p. 3124, Aug. 2019, doi: 10.3390/en12163124.

[6] M. A. Lackner and G. Van Kuik, "A comparison of smart rotor control approaches using trailing edge flaps and individual pitch control," *Wind Energ.*, vol. 13, nos. 2–3, pp. 117–134, Mar. 2010, doi: 10.1002/we.353.

[7] W. Zhang, R. Liu, Y. Wang, Y. Wang, and X. Zhang, "Smart rotor with trailing edge flap considering bend–twist coupling and aerodynamic damping: Modeling and control," *J. Vib. Acoust.*, vol. 141, no. 4, Aug. 2019, doi: 10.1115/1.4043240.

[8] S. Basualdo, "Load alleviation on wind turbine blades using variable airfoil geometry," *Wind Eng.*, vol. 29, no. 2, pp. 169–182, Mar. 2005.

[9] C. Bak, M. Gaunaa, P. Andersen, T. Buhl, P. Hansen, K. Clemmensen, and R. Moeller, "Wind tunnel test on wind turbine airfoil with adaptive trailing edge geometry," in *Proc. 45th AIAA Aerosp. Sci. Meeting Exhib.*, Jan. 2007, p. 1016.

[10] P. B. Andersen, M. Gaunaa, C. Bak, and M. H. Hansen, "A dynamic stall model for airfoils with deformable trailing edges," *Wind Energy*, vol. 12, no. 8, pp. 734–751, Nov. 2009, doi: 10.1002/we.326.

[11] T. Buhl, M. Gaunaa, and C. Bak, "Potential load reduction using airfoils with variable trailing edge geometry," *J. Sol. Energy Eng.*, vol. 127, no. 4, pp. 503–516, Nov. 2005.

[12] M. Gaunaa, "Unsteady 2D potential-flow forces on a thin variable geometry airfoil undergoing arbitrary motion," Risø Nat. Lab., Roskilde, Denmark, Tech. Rep. Risø–R–1478(EN), Jul. 2006.

[13] J. C. Berg, B. R. Resor, J. A. Paquette, and J. White, "SMART wind turbine rotor: Design and field test," Sandia Nat. Lab., Albuquerque, NM, USA, Tech. Rep. SAND2014-0681, Nov. 2014.

[14] J. C. Berg, M. F. Barone, and N. C. Yoder, "SMART wind turbine rotor: Data analysis and conclusions," Sandia Nat. Lab., Albuquerque, NM, USA, Tech. Rep. SAND2014-0712, Nov. 2014.

[15] W. Zhang, Y. Wang, R. Liu, H. Liu, and X. Zhang, "Unsteady aerodynamic modeling and control of the wind turbine with trailing edge flap," *J. Renew. Sustain. Energy*, vol. 10, no. 6, Nov. 2018, Art. no. 063304, doi: 10.1063/1.5052023.

[16] D. Castaignet, T. Barlas, T. Buhl, N. Poulsen, J. Wedel-Heinen, N. Olesen, C. Bak, and T. Kim, "Full-scale test of trailing edge flaps on a Vestas V27 wind turbine: Active load reduction and system identification," *Wind Energy*, vol. 17, no. 4, pp. 549–564, Apr. 2014, doi: 10.1002/we.1589.

[17] A. Abdelrahman and D. A. Johnson, "Development of a wind turbine test rig and rotor for trailing edge flap investigation: Static flap angles case," *J. Phys., Conf. Ser.*, vol. 524, Jun. 2014, Art. no. 012059.

[18] A. W. Hulskamp and A. Beukers, "Design of a wind tunnel scale model of an adaptive wind turbine blade for active aerodynamic load control experiments," presented at the 16th Int. Conf. Compos. Mater., Tokyo, Japan, 2007.

[19] A. W. Hulskamp, J. W. Van Wingerden, T. Barlas, H. Champliaud, G. A. M. Van Kuik, H. E. N. Bersee, and M. Verhaegen, "Design of a scaled wind turbine with a smart rotor for dynamic load control experiments," *Wind Energ.*, vol. 14, no. 3, pp. 339–354, Apr. 2011, doi: 10.1002/we.424.

[20] J.-W. Van Wingerden, A. Hulskamp, T. Barlas, I. Houtzager, H. Bersee, G. van Kuik, and M. Verhaegen, "Two-degree-of-freedom active vibration control of a prototyped 'smart' rotor," *IEEE Trans. Control Syst. Technol.*, vol. 19, no. 2, pp. 284–296, Mar. 2011, doi: 10.1109/tcst.2010.2051810.

[21] J. K. Rice and M. Verhaegen, "Robust and distributed control of a smart blade," *Wind Energy*, vol. 13, nos. 2–3, pp. 103–116, Mar. 2010, doi: 10.1002/we.362.

[22] P. B. Anderson, "Advanced load alleviation for wind turbines using adaptive trailing edge flaps: Sensoring and control," Ph.D. dissertation, Dept. Delhi Technol. Univ., New Delhi, India, 2006.

[23] T. Barlas, G. Van Der Veen, and G. Van Kuik, "Model predictive control for wind turbines with distributed active flaps: Incorporating inflow signals and actuator constraints," *Wind Energy*, vol. 15, no. 5, pp. 757–771, Jul. 2012, doi: 10.1002/we.503.

[24] L. Bergami and N. K. Poulsen, "A smart rotor configuration with linear quadratic control of adaptive trailing edge flaps for active load alleviation," *Wind Energy*, vol. 18, no. 4, pp. 625–641, Apr. 2015, doi: 10.1002/we.1716.

[25] A. Fischer and H. A. Madsen, "Investigation of the theoretical load alleviation potential using trailing edge flaps controlled by inflow data," *Wind Energy*, vol. 19, no. 9, pp. 1567–1583, Sep. 2016, doi: 10.1002/we.1937.

[26] J. Smit, L. O. Bernhammer, S. T. Navalkar, L. Bergami, and M. Gaunaa, "Sizing and control of trailing edge flaps on a smart rotor for maximum power generation in low fatigue wind regimes," *Wind Energy*, vol. 19, no. 4, pp. 607–624, Apr. 2016, doi: 10.1002/we.1853.

[27] W. Zhang, X. Bai, Y. Wang, Y. Han, and Y. Hu, "Optimization of sizing parameters and multi-objective control of trailing edge flaps on a smart rotor," *Renew. Energy*, vol. 129, pp. 75–91, Dec. 2018, doi: 10.1016/j.renene.2018.05.091.

[28] J. M. Jonkman and M. Buhl, "FAST user's guide," NREL, Golden, CO, USA, Tech. Rep. NREL/EL-500-38230, 2005.

[29] P. B. Andersen, L. Henriksen, M. Gaunaa, C. Bak, and T. Buhl, "Deformable trailing edge flaps for modern megawatt wind turbine controllers using strain gauge sensors," *Wind Energy*, vol. 13, nos. 2–3, pp. 193–206, Mar. 2010, doi: 10.1002/we.371.

[30] L. Wang, X. Liu, and A. Kolios, "State of the art in the aeroelasticity of wind turbine blades: Aeroelastic modelling," *Renew. Sustain. Energy Rev.*, vol. 64, pp. 195–210, Oct. 2016, doi: 10.1016/j.rser.2016.06.007.

[31] L. Ma, X. Wang, J. Zhu, and S. Kang, "Effect of DBD plasma excitation characteristics on turbulent separation over a hump model," *Plasma Sci. Technol.*, vol. 20, no. 10, Oct. 2018, Art. no. 105503, doi: 10.1088/2058-6272/aacdf0.

[32] E. Jost, A. Fischer, and T. Lutz, "CFD studies of a 10 MW wind turbine equipped with active trailing edge flaps," presented at the 10th PhD Seminar Wind Energy Eur., Orleans, France, 2014.

[33] H. Kamliya Jawahar, Q. Ai, and M. Azarpeyvand, "Experimental and numerical investigation of aerodynamic performance for airfoils with morphed trailing edges," *Renew. Energy*, vol. 127, pp. 355–367, Nov. 2018, doi: 10.1016/j.renene.2018.04.066.

[34] M. Gaumond, P.-E. Réthoré, S. Ott, A. Peña, A. Bechmann, and K. S. Hansen, "Evaluation of the wind direction uncertainty and its impact on wake modeling at the Horns Rev offshore wind farm," *Wind Energy*, vol. 17, no. 8, pp. 1169–1178, Aug. 2014, doi: 10.1002/we.1625.

[35] J. Jonkman, S. Butterfield, W. Musial, and G. Scott, "Definition of a 5-MW reference wind turbine for offshore system development," Nat. Renew. Energy Lab., Golden, CO, USA, Tech. Rep. NREL/TP-500-38060, 2009.

[36] *ANSYS FLUENT in ANSYS Workbench User's Guide*, Fluent, Canonsburg, PA, USA, 2013.

[37] B. Dose, H. Rahimi, I. Herráez, B. Stoevesandt, and J. Peinke, "Fluid-structure coupled computations of the NREL 5 MW wind turbine by means of CFD," *Renew. Energy*, vol. 129, pp. 591–605, Dec. 2018, doi: 10.1016/j.renene.2018.05.064.

[38] L. J. Vermeer, J. N. Sørensen, and A. Crespo, "Wind turbine wake aerodynamics," *Prog. Aerosp. Sci.*, vol. 39, nos. 6–7, pp. 467–510, Aug. 2003, doi: 10.1016/S0376-0421(03)00078-2.

[39] T. Göçmen, P. van der Laan, P.-E. Réthoré, A. P. Diaz, G. C. Larsen, and S. Ott, "Wind turbine wake models developed at the technical University of Denmark: A review," *Renew. Sustain. Energy Rev.*, vol. 60, pp. 752–769, Jul. 2016, doi: 10.1016/j.rser.2016.01.113.

[40] X. Wang, Y. Liu, L. Wang, L. Ding, and H. Hu, "Numerical study of nacelle wind speed characteristics of a horizontal axis wind turbine under time-varying flow," *Energies*, vol. 12, no. 20, p. 3993, Oct. 2019, doi: 10.3390/en12203993.

[41] F. Zahle, N. N. Sørensen, and J. Johansen, "Wind turbine rotor-tower interaction using an incompressible overset grid method," *Wind Energy*, vol. 12, no. 6, pp. 594–619, Sep. 2009, doi: 10.1002/we.327.

[42] A. Abraham, T. Dasari, and J. Hong, "Effect of turbine nacelle and tower on the near wake of a utility-scale wind turbine," *J. Wind Eng. Ind. Aerodyn.*, vol. 193, Oct. 2019, Art. no. 103981, doi: 10.1016/j.jweia.2019.103981.

[43] F. González-Longatt, P. Wall, and V. Terzija, "Wake effect in wind farm performance: Steady-state and dynamic behavior," *Renew. Energy*, vol. 39, no. 1, pp. 329–338, Mar. 2012, doi: 10.1016/j.renene.2011.08.053.

[44] N. J. Choi, S. H. Nam, J. H. Jeong, and K. C. Kim, "Numerical study on the horizontal axis turbines arrangement in a wind farm: Effect of separation distance on the turbine aerodynamic power output," *J. Wind Eng. Ind. Aerodyn.*, vol. 117, pp. 11–17, Jun. 2013, doi: 10.1016/j.jweia.2013.04.005.

[45] *STAR-CCM+ V13.02 User's Guide*, Siemens PLM Softw., Plano, TX, USA, 2018.

[46] *ANSYS ICEM CFD User Manual*, ANSYS, Canonsburg, PA, USA, 2012.

[47] F. R. Menter, "Two-equation eddy-viscosity turbulence models for engineering applications," *AIAA J.*, vol. 32, no. 8, pp. 1598–1605, Aug. 1994.

[48] J.-O. Mo, A. Choudhry, M. Arjomandi, and Y.-H. Lee, "Large eddy simulation of the wind turbine wake characteristics in the numerical wind tunnel model," *J. Wind Eng. Ind. Aerodyn.*, vol. 112, pp. 11–24, Jan. 2013, doi: 10.1016/j.jweia.2012.09.002.

YUANYUAN WANG received the B.S. degree from North China Electric Power University, Beijing, China, in 2017, where she is currently pursuing the M.S. degree. Her research interests include computational fluid dynamics simulation and control of smart rotor.

YANGZHI SHEN received the B.S. degree from North China Electric Power University, Beijing, China, in 2017, where he is currently pursuing the M.S. degree. His research interests include computational fluid dynamics simulation and control of smart rotor.

YANG WANG received the B.S. degree from the North China Institute of Science and Technology, China, in 2016. He is currently pursuing the master's degree with North China Electric Power University, China. His research interests include computational fluid dynamics simulation and control of smart rotor.

YUE XU received the M.A.Eng. degree from North China Electric Power University, Beijing, China, in 2015. She was with the CSSC Systems Engineering Research Institute. She is currently an Engineer with China Shipbuilding IT Company Ltd. Her research interests include hydrodynamic analysis, ship electronic information systems, big data analysis, and artificial intelligence.

WENGUANG ZHANG received the B.Eng. and Ph.D. degrees from Beihang University, Beijing, China, in 1999 and 2009, respectively. He is currently an Associate Professor with the State Key Laboratory of Alternate Electrical Power System with Renewable Energy Sources, North China Electric Power University, Beijing. His research interests include modeling and control of smart rotor and complex system control.

XINYU ZHANG received the M.S.E. degree from the Dalian University of Technology, China, in 2016. She was with the CSSC Systems Engineering Research Institute. She is currently an Engineer with China Shipbuilding IT Company Ltd. Her research interests include hydrodynamic analysis and ship electronic information systems.

• • •